



# Carbothermal activation synthesis of 3D porous g-C<sub>3</sub>N<sub>4</sub>/carbon nanosheets composite with superior performance for CO<sub>2</sub> photoreduction

Yangang Wang<sup>a,\*</sup>, Qineng Xia<sup>a</sup>, Xia Bai<sup>a,c</sup>, Zhigang Ge<sup>a</sup>, Qian Yang<sup>d</sup>, Chaochuang Yin<sup>c</sup>, Shifei Kang<sup>c</sup>, Mingdong Dong<sup>d</sup>, Xi Li<sup>a,b,\*</sup>

<sup>a</sup> College of Biological Chemical Science and Engineering, Jiaying University, Jiaying 314001, China

<sup>b</sup> Department of Environmental Science and Engineering, Fudan University, Shanghai 200433, China

<sup>c</sup> Department of Environmental Science and Engineering, University of Shanghai for Science and Technology, Shanghai 200093, China

<sup>d</sup> Interdisciplinary Nanoscience Center (iNANO), Aarhus University, Gustav Wieds Vej 14, 8000 Aarhus C, Denmark

## ARTICLE INFO

### Keywords:

Graphene-like nanosheets

g-C<sub>3</sub>N<sub>4</sub>/C composite

3D porous

Carbon-oxygen groups

CO<sub>2</sub> photoreduction

## ABSTRACT

3D porous nanosheets composite comprised of graphitic carbon nitride (g-C<sub>3</sub>N<sub>4</sub>) and carbon was prepared by a simple pyrolysis and subsequent carbothermal activation method for the first time. The morphology and structural properties of obtained 3D porous g-C<sub>3</sub>N<sub>4</sub>/C nanosheets composite was systematically investigated. It was found that the morphology of the g-C<sub>3</sub>N<sub>4</sub>/C composite evolved from scroll-like structure to 3D porous nanosheets with ultrathin layer after 6 h activation, meanwhile, the specific surface area and pore volume were significantly increased. Such 3D porous nanosheets like these can function as effective catalysts for a range of gas-phase photocatalytic reactions such as photocatalytic reduction of CO<sub>2</sub> with H<sub>2</sub>O vapor to produce value-added fuels. As a demonstration, outstanding photocatalytic activity was achieved on this 3D porous g-C<sub>3</sub>N<sub>4</sub>/C nanosheets composite, where ultra-high CO and CH<sub>4</sub> yield of 229 and 112 μmol g<sup>-1</sup>-cat, respectively, were acquired under 7 h simulated solar irradiation, which were 25-fold better than that of bulk g-C<sub>3</sub>N<sub>4</sub>. The excellent photocatalytic performance should be attributed to the advantageous structural and compositional features.

## 1. Introduction

Since the discovery of CO<sub>2</sub> photoreduction in a semiconductor aqueous suspension [1], searching and optimizing high-efficiency photocatalysts for converting CO<sub>2</sub> into value-added resources that can relieve energy crisis and environmental problems has attracted considerable attention worldwide. Up to now, relevant research is mostly focused on metal oxide semiconductor photocatalysts. However, economic cost concern of these metal-containing photocatalysts have become a huge barrier against their widespread applications. Given the requirements of low cost, scalability and nontoxicity or environmental issues, the metal-free materials have manifested as fascinating green alternatives with promising effectiveness in multifaceted applications, such as energy conversion and storage [2,3], and environmental remediation [4–6]. Recently, great efforts have been devoted to preparation of metal-free carbon nitride (C<sub>3</sub>N<sub>4</sub>) materials and their use as photocatalysts in solar fuel conversion, pollutant degradation and CO<sub>2</sub> reduction due to their novel structures and unique properties [7–12]. Graphitic C<sub>3</sub>N<sub>4</sub> (g-C<sub>3</sub>N<sub>4</sub>) is indeed a novel metal-free visible-light

photocatalyst characterized by extraordinary properties, an appealing electronic structure and a medium band gap (2.7 eV) [13]. Nevertheless, the activity of bulk g-C<sub>3</sub>N<sub>4</sub> in CO<sub>2</sub> photoreduction to value-added fuels is still very low on account of its small specific surface area (SSA), high recombination of photo-generated electron–hole pairs and low electron conductivity [14–22]. Undoubtedly, these properties of g-C<sub>3</sub>N<sub>4</sub> is closely related to the morphology and structure. Therefore, research on structural design and morphologic optimization of bulk g-C<sub>3</sub>N<sub>4</sub> is highly demanded so as to weaken the adverse effects resulting from the small SSA and low electron conductivity [23].

Ultrathin nanosheets, involving van der Waals interaction between adjacent sheets and characterized by unique optical and electronic properties, have attracted extensive attention in the fields of sensors, electronics, catalysis, and energy conversion [24]. As for the photocatalytic application, this characteristic structure can increase the SSA with abundant reactive sites and shorten bulk diffusion length to accelerate the transfer and separation of charge carriers. Theoretically, g-C<sub>3</sub>N<sub>4</sub> has a layered structure that consists of highly-ordered tri-s-triazine moiety sheets connected through planar tertiary amino groups

\* Corresponding author at: College of Biological Chemical Science and Engineering, Jiaying University, Jiaying 314001, China.

\*\* Corresponding author.

E-mail addresses: [ygwang8136@mail.jzjxu.edu.cn](mailto:ygwang8136@mail.jzjxu.edu.cn) (Y. Wang), [xi\\_li@fudan.edu.cn](mailto:xi_li@fudan.edu.cn) (X. Li).

<https://doi.org/10.1016/j.apcatb.2018.08.018>

Received 16 March 2018; Received in revised form 7 July 2018; Accepted 6 August 2018

Available online 07 August 2018

0926-3373/ © 2018 Elsevier B.V. All rights reserved.

[25]. Since layers are connected by weak van der Waals force analogous to graphite, academically it is feasible to obtain g-C<sub>3</sub>N<sub>4</sub> nanosheets from bulk g-C<sub>3</sub>N<sub>4</sub>, thus further expanding its applications [26]. Generally, the properties and photocatalytic activity of g-C<sub>3</sub>N<sub>4</sub> nanosheets are more competitive with multilayer stacked bulk g-C<sub>3</sub>N<sub>4</sub> mainly in two aspects: 1) The electron and hole mobility in nanosheets, on account of the quantum confinement effect, is significantly greater than that in the bulk, as proved in the study on graphene [27]; 2) The surface area of nanosheets is much larger than that of bulk, which largely contributes to light harvest and charge carrier transport. To date, tremendous endeavors have been made to preparation of g-C<sub>3</sub>N<sub>4</sub> nanosheets using various methods, including thermal oxidation “etching” and liquid exfoliation [28]. However, most methods are limited by low yield and technical challenges [29,30]. On the other hand, like many other photocatalysts, g-C<sub>3</sub>N<sub>4</sub> alone exhibits very low electrical conductivity which is one of suppression factors for photocatalytic efficiency. Generally, the integration of well-conductive materials into g-C<sub>3</sub>N<sub>4</sub> can further lower the redox potential of reaction at the corresponding active sites and effectively accelerate electron-hole pair separation and transport. Among various materials, carbonaceous materials (e.g. carbon nanotubes [31], fullerene [32], graphene [33], carbon black [34,35], and carbon quantum dots [36]) have been increasingly used lately to enhance charge carriers transfer. Our recent result also showed that introduction of hybrid carbon in g-C<sub>3</sub>N<sub>4</sub> can remarkably increase its photocatalytic performance such as in the reduction of CO<sub>2</sub> with H<sub>2</sub>O [37].

Herein, novel 3D porous graphitic carbon nitride/carbon (g-C<sub>3</sub>N<sub>4</sub>/C) nanosheets composite (denoted as 3D g-C<sub>3</sub>N<sub>4</sub>/C-NS) was synthesized for the first time by using a simple “carbothermal activation” method based on our previous hybrid graphitic carbon nitride and carbon composite (H-g-C<sub>3</sub>N<sub>4</sub>/C) which was prepared by one-step pyrolysis of a mixture of melamine and natural soybean oil at 600 °C under N<sub>2</sub> atmosphere (Fig. 1). It is found that the hybrid carbon in the composite is critical to the formation of 3D porous structure during the activation process. In comparison to H-g-C<sub>3</sub>N<sub>4</sub>/C and bulk g-C<sub>3</sub>N<sub>4</sub>, the obtained 3D g-C<sub>3</sub>N<sub>4</sub>/C-NS has the following advantages: (1) 3D porous architecture with hierarchical mesostructure allows effective gas reactants or products diffusion/transfer; (2) high specific surface area with plentiful exposed functional groups provides a high surface gas reactant (e.g. CO<sub>2</sub>) concentration and more active sites; (3) graphene-like nanosheets with 3D interconnecting structure can serve as efficient light management to enhance light trapping/utilization; (4) a lower recombination rate of the photogenerated electron-hole pairs is acquired because of the improved surface properties and the quantum confinement effect of graphene-like nanosheets. Consequently, the resulted 3D g-C<sub>3</sub>N<sub>4</sub>/C-NS demonstrated an exceptionally high performance for the photoreduction of CO<sub>2</sub> with H<sub>2</sub>O to produce value-added fuels (such as CH<sub>4</sub> and CO) under simulated solar irradiation.

## 2. Experimental

### 2.1. Materials preparation

The typical synthesis process of 3D porous g-C<sub>3</sub>N<sub>4</sub>/C nanosheets composite is very simple. Specifically, melamine powder (purchased from Sinopharm Chemical Reagent Co.) and soybean oil at the weight ratio of 6:1 were ground together for 10 min in an agate mortar to form a homogenous mixture. Then the mixture was transferred into a temperature-controlled tube furnace and annealed at 600 °C for 2 h with a heating ramp of 2 °C min<sup>-1</sup> under N<sub>2</sub> flow. After cooling to room temperature, the obtained black powder (denoted as H-g-C<sub>3</sub>N<sub>4</sub>/C) was transferred into a 50 mL alumina crucible with a cover and activated to 550 °C under static air for 6 h to form 3D porous nanosheets. The final 3D porous nanosheets composite was named as 3D g-C<sub>3</sub>N<sub>4</sub>/C-NS for convenience. For the control experiment, a bulk g-C<sub>3</sub>N<sub>4</sub> was synthesized via thermal polycondensation of melamine powder at 600 °C according to a literature [19].

### 2.2. Materials characterization

X-ray diffraction patterns were operated on a powder X-ray diffractometer (Bruker D8 Advance, Germany) with CuKα<sub>1</sub> radiation (λ = 1.5406 Å). Scanning electron microscopy (SEM) was taken using a Zeiss Ultra 55 field emission scanning electron microscope with an acceleration voltage of 25 kV. Transmission electron microscope (TEM) images were performed on a JEOL JEM-2010 electron microscope operating at an acceleration voltage of 200 kV. Thermogravimetric analysis (TG) was conducted on a PerkinElmer STA-8000 analyzer (America), and the experiment temperature ranged from 50 °C to 1200 °C at a heating rate of 10 °C min<sup>-1</sup> in Ar atmosphere. Nitrogen adsorption-desorption isotherm at 77 K was measured on a BeiShiDe 3H-2000PS4 apparatus to determine the Brunauer–Emmett–Teller (BET) surface area, pore volume, porosity, and BJH pore size distribution. Elemental analyses (C, N, H) were measured by a Euro EA3000 elemental analyser (EA, Euro Vector S.P.A., Italy). X-ray photoelectron spectroscopy (XPS) was recorded on an RBO upgraded PHI-5000C ESCA system (Pekin Elmer) using monochromated Al Kα X-rays (hν = 1486.6 eV) with radiation at 250 W. Fourier transform infrared FTIR spectra were acquired from a Nicolet iS10 spectrometer using the KBr pellet technique. Photoluminescence (PL) spectra were performed at room temperature on a Fluorescence Spectrophotometer (Hitachi F-7000, Japan). EIS and photocurrent measurements were carried out on an electrochemical analyzer (CHI 660E Instruments) based on a conventional three-electrode system in which the prepared sample film was used as the working electrode, a Pt flake as the counter electrode, and Ag/AgCl as the reference electrode.

### 2.3. CO<sub>2</sub> adsorption measurements

The CO<sub>2</sub> adsorption isotherms of the samples were measured using a Quantachrome NOVA2000e static volumetric analyzer at 30 °C. Prior to each adsorption experiment, the sample was degassed for 6 h at 160 °C

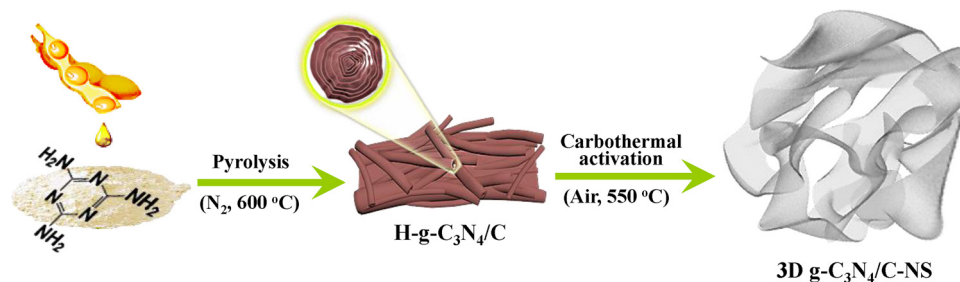


Fig. 1. Schematic to show the synthesis process of 3D porous g-C<sub>3</sub>N<sub>4</sub>/C nanosheets composite.

ensuring that the residual pressure fell below 0.05 mbar and then cooled down to the required temperature, following by introduction of pure  $\text{CO}_2$  into the system. The  $\text{CO}_2$  adsorption capacity in terms of adsorbed volume under standard temperature and pressure was then recorded.

## 2.4. Photocatalytic measurements

The photocatalytic reduction of  $\text{CO}_2$  experiments were carried out in a home-made Teflon-lined stainless steel reactor (volume: 2700 mL) with a quartz window at the top of light irradiation. In each experiment, 0.1 g of catalyst powder was dispersed on the stainless omentum which was fixed in the center of reactor. Before the reaction, the reactor was vacuum-treated for several times, and then purged with the  $\text{CO}_2 + \text{H}_2\text{O}$  mixture at about  $20 \text{ ml min}^{-1}$  for 3 h until reaching the adsorption-desorption equilibrium. Then the experiment was started by tightly closing the reactor and switching on the Xe arc lamp (500 W). The substrate was about 15 cm away from the Xe arc lamp, the reaction temperature and pressure were maintained at  $30^\circ\text{C}$  and 110 K Pa, respectively. In order to control the reaction temperature, the Xe arc lamp was placed in a cold trap and the whole reactor system was in the air circulation. The gas-phase products were collected every hour and analyzed online by gas chromatography (LH 9890B) equipped with flame ionization detector (FID) and thermal conductivity detector (TCD).

## 3. Results and discussion

### 3.1. Characteristics of materials

Fig. 2a gives the photographs of the synthesized 3D  $\text{g-C}_3\text{N}_4/\text{C-NS}$ ,  $\text{H-g-C}_3\text{N}_4/\text{C}$ , and bulk  $\text{g-C}_3\text{N}_4$ . It is reasonable that the bright yellow color of  $\text{g-C}_3\text{N}_4$  becomes black after introducing the hybrid carbon. Compared with the bulk  $\text{g-C}_3\text{N}_4$  and  $\text{H-g-C}_3\text{N}_4/\text{C}$ , the volume of 3D  $\text{g-C}_3\text{N}_4/\text{C-NS}$

$\text{C-NS}$  is much larger under the same weight, indicating the formation of fluffy state nanosheets after activation. The same characteristic is observed for  $\text{g-C}_3\text{N}_4$  nanosheets prepared from liquid exfoliation [38,39]. Such structural change may enhance the light absorption and alter the optical as well as the surface chemical properties of the  $\text{g-C}_3\text{N}_4/\text{C}$  composite. The XRD patterns of three samples are shown in Fig. 2b. The bulk  $\text{g-C}_3\text{N}_4$  has two primary characteristic peaks: (i) the strong shoulder peak at  $2\theta = 27$  ( $d = 0.326 \text{ nm}$ ) originating from the (002) interlayer stacking of aromatic systems; (ii) the peak at  $2\theta = 13$  ( $d = 0.663 \text{ nm}$ ) derived from the in-plane repeated unites [40]. Obviously, both  $\text{H-g-C}_3\text{N}_4/\text{C}$  and 3D  $\text{g-C}_3\text{N}_4/\text{C-NS}$  exhibit two peaks which are consistent with the parent bulk  $\text{g-C}_3\text{N}_4$ , implying that they basically have the similar crystal structure as bulk  $\text{g-C}_3\text{N}_4$ . However, the intensity of the (100) peak is obviously weakened after carbothermal activation, suggesting the activation treatment decreased the planar size of the layers and partially destroyed the crystal structure [41,42]. Moreover, as for close-up view of the (002) diffraction peak in the inset of Fig. 2b, a lower  $2\theta$  value are observed for both  $\text{g-C}_3\text{N}_4/\text{C}$  samples. This crystal lattice distortion induced by hybrid carbon modification not only results in the introduction of defects in  $\text{g-C}_3\text{N}_4$ , but also shortens the correlation length of interlayer periodicity of the CN motifs [43]. However, no distinct carbon-related diffraction peaks are observed from Fig. 2b, indicating the formation of amorphous carbon. The weight percentage of carbon obtained by TG analysis (Fig. S1) in 3D  $\text{g-C}_3\text{N}_4/\text{C-NS}$  and  $\text{H-g-C}_3\text{N}_4/\text{C}$  is calculated to be about 16.2% and 4.1%, respectively. The textural parameters of three samples were further investigated through  $\text{N}_2$  adsorption-desorption isotherms. The 3D  $\text{g-C}_3\text{N}_4/\text{C-NS}$  show a typical type-IV isotherm with  $\text{H}_3$ -type hysteresis loop as a consequence of capillary condensation in the  $P/P_0$  range of 0.55–0.95 (Fig. 2c) which indicates its porous property [28], while no obvious hysteresis loops are found on the isotherms of both bulk  $\text{g-C}_3\text{N}_4$  and  $\text{H-g-C}_3\text{N}_4/\text{C}$  samples. The pore size distributions determined from the adsorption branches of the isotherms using the Barret–Joyner–Halenda (BJH) method are given in Fig. 2d. It can be seen that the 3D  $\text{g-C}_3\text{N}_4/\text{C-NS}$

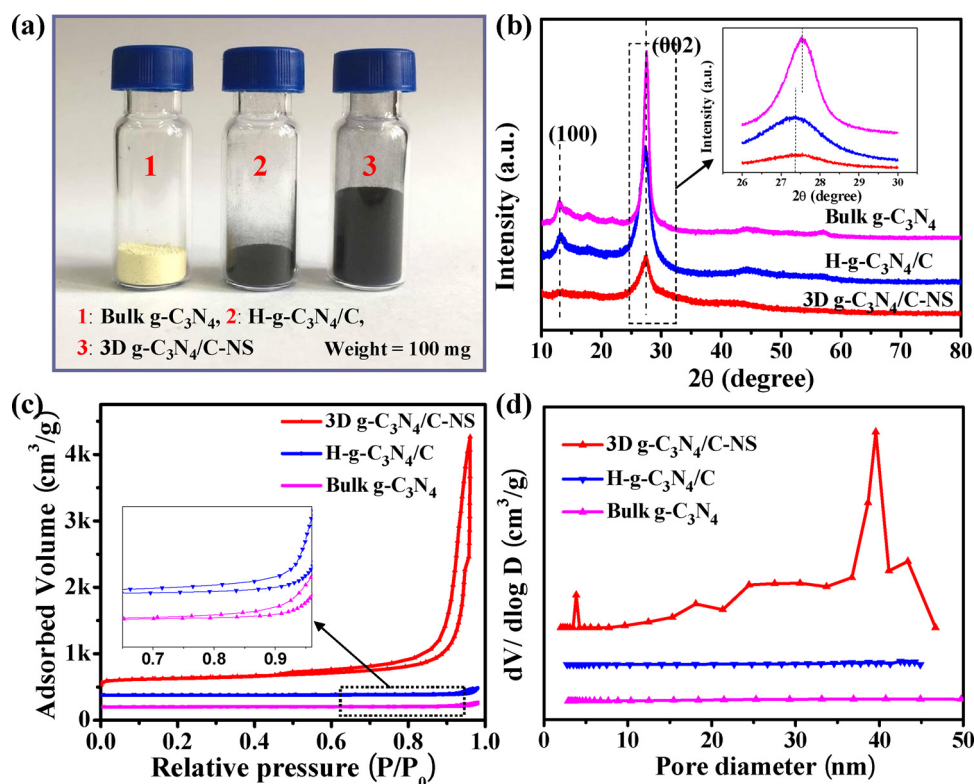


Fig. 2. (a) photograph, (b) XRD patterns, (c)  $\text{N}_2$  adsorption-desorption isotherms and (d) corresponding pore size distribution curves of 3D  $\text{g-C}_3\text{N}_4/\text{C-NS}$ ,  $\text{H-g-C}_3\text{N}_4/\text{C}$  and bulk  $\text{g-C}_3\text{N}_4$ .



**Table 1**  
Textural properties of the 3D g-C<sub>3</sub>N<sub>4</sub>/C-NS, H-g-C<sub>3</sub>N<sub>4</sub>/C and bulk g-C<sub>3</sub>N<sub>4</sub>.

Sample	Elemental analysis				XPS analysis				Surface area (m <sup>2</sup> /g)	Pore size (nm)	Pore volume (cm <sup>3</sup> /g)
	C (wt. %)	N (wt. %)	H (wt. %)	C/N (atomic ratio)	C (at. %)	N (at. %)	O (at. %)	C/N (atomic ratio)			
3D g-C <sub>3</sub> N <sub>4</sub> /C-NS	47.84	49.40	2.76	1.13	48.83	45.64	5.53	1.07	454.2	4, 39	5.825
H-g-C <sub>3</sub> N <sub>4</sub> /C	40.96	56.83	2.21	0.84	44.57	53.69	1.74	0.83	11.1	/	0.166
Bulk g-C <sub>3</sub> N <sub>4</sub>	39.07	59.19	1.74	0.77	42.86	56.40	0.73	0.76	7.6	/	0.108

C<sub>3</sub>N<sub>4</sub>/C-NS possesses hierarchical bimodal mesopores centered at 4 and 39 nm, respectively. These mesopores should originate from the stacking of ultrathin g-C<sub>3</sub>N<sub>4</sub>/C nanosheets. In contrast, no apparent pore size distribution is observed in both bulk g-C<sub>3</sub>N<sub>4</sub> and H-g-C<sub>3</sub>N<sub>4</sub>/C. As expected, the BET surface area and pore volume are dramatically increased for the 3D g-C<sub>3</sub>N<sub>4</sub>/C-NS with the values of 454.2 m<sup>2</sup>/g and 5.825 cm<sup>3</sup>/g, respectively (Table 1), much higher than that of original H-g-C<sub>3</sub>N<sub>4</sub>/C (11.1 m<sup>2</sup>/g and 0.166 cm<sup>3</sup>/g, respectively), which should be attributed to the hybrid carbon in the g-C<sub>3</sub>N<sub>4</sub>/C composites in favor of expanding the stacked g-C<sub>3</sub>N<sub>4</sub>/C layers and forming 3D porous structure during the carbothermal activation process.

The morphology and microstructure of the synthesized samples were investigated by SEM and TEM images. As shown in Fig. S2, the SEM images of bulk g-C<sub>3</sub>N<sub>4</sub> represent typical compact monolith-like morphology. After introducing hybrid carbon in g-C<sub>3</sub>N<sub>4</sub>, scroll-like substructures appear in the stacking layers (Fig. S3), which are consistent with our previous research [37]. Interestingly, the scroll-like structures are unfolded gradually like blooming and produce large amounts of crumpled nanosheets which randomly aggregate and entangle with

each other, and finally form a well-defined 3D structure for 3D g-C<sub>3</sub>N<sub>4</sub>/C-NS (Fig. 3a and b). TEM images in Figs. 3c–e and S4 reveal that obtained nanosheets have graphene-like laminar structure with the thickness of about 4 nm, meanwhile, some slit-like mesopores can be distinguished on these nanosheets, which is agreement with the result of BJH analysis. Such 3D porous architecture can function as light management to enhance the light trapping inside active sites of g-C<sub>3</sub>N<sub>4</sub> photocatalyst [44–46], meanwhile, the ultrathin graphene-like nanosheets is a typical transparent substrate at microscale level which can effectively increase the light scattering and utilization rate of the trapped light during photocatalytic process. Moreover, the TEM image of the typical area and the corresponding EDX elemental maps are shown in Fig. 3f–i. These results confirm the homogenous distribution of C, N and a small quantity of O elements on the graphene-like nanosheets. The existence of O elements perhaps origin from the oxidation of a little C element or the defect of partial g-C<sub>3</sub>N<sub>4</sub>.

The chemical structures of the samples were further characterized by Fourier transform infrared (FTIR). As shown in Fig. 4a, the 3D g-C<sub>3</sub>N<sub>4</sub>/C-NS shows a characteristic IR spectrum analogous to bulk g-

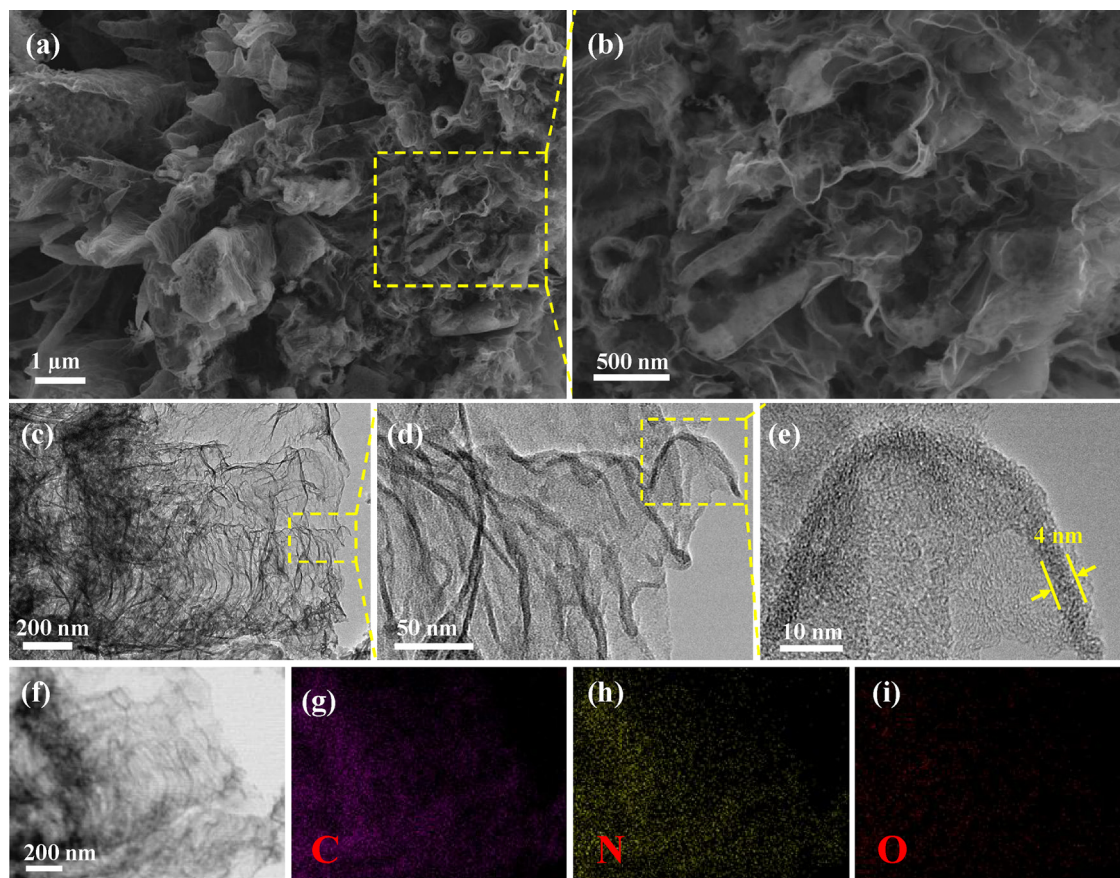


**Fig. 3.** Morphology and microstructure. a, b) SEM images of the 3D g-C<sub>3</sub>N<sub>4</sub>/C-NS showing the 3D porous nanosheets. c–e) TEM and HRTEM images of the 3D g-C<sub>3</sub>N<sub>4</sub>/C-NS, showing the nanosheets have graphene-like laminar structure with the thickness of about 4 nm. f–i) TEM image of the 3D g-C<sub>3</sub>N<sub>4</sub>/C-NS and corresponding EDX elemental maps, showing the uniform distribution of g-C<sub>3</sub>N<sub>4</sub> on the graphene-like nanosheets.

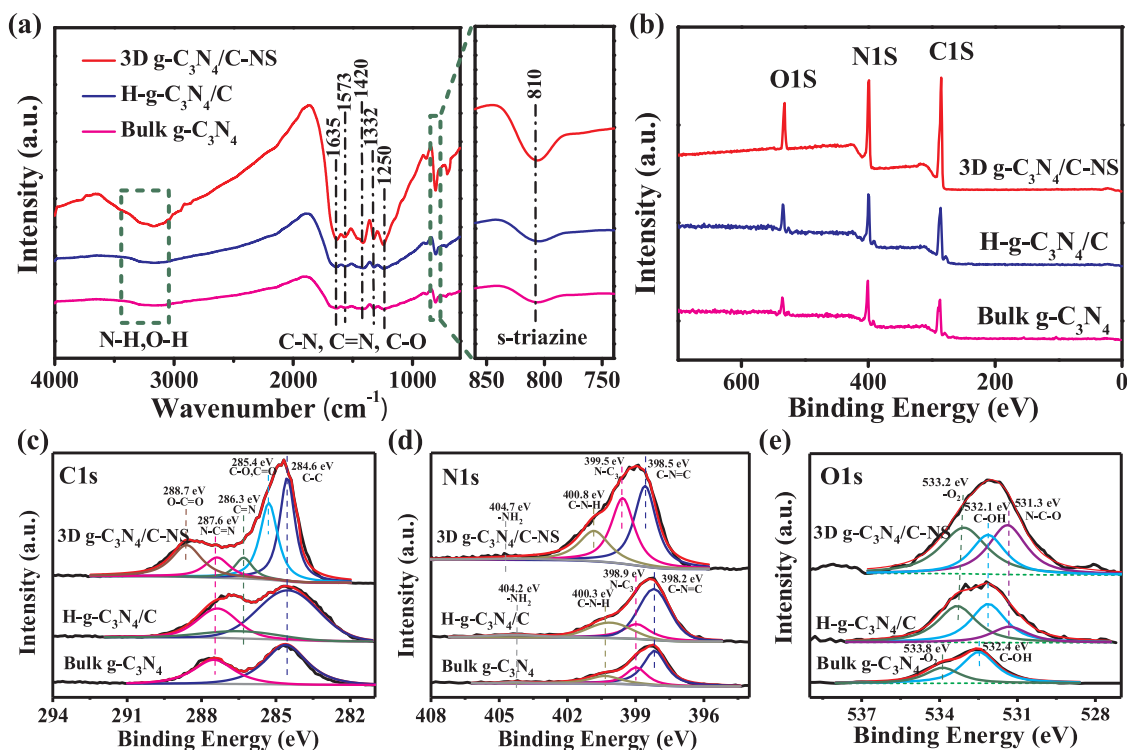


**Fig. 4.** FTIR spectra (a) and XPS survey spectra (b) of 3D g-C<sub>3</sub>N<sub>4</sub>/C-NS, H-g-C<sub>3</sub>N<sub>4</sub>/C and bulk g-C<sub>3</sub>N<sub>4</sub>. High-resolution XPS spectra of C 1s (c), N 1s (d), and O 1s (e) of all samples.

C<sub>3</sub>N<sub>4</sub> and H-g-C<sub>3</sub>N<sub>4</sub>/C, indicating the structural integrity of g-C<sub>3</sub>N<sub>4</sub> remained intact after carbothermal activation. The broad absorption peak ranging from 2800 to 3400 cm<sup>-1</sup> is the stretching ascribed to the vibrational modes of the N–H (amino groups) and O–H (adsorbed hydroxyl species), respectively. The vibration characteristic detected in the 1200–1700 cm<sup>-1</sup> frequency region of IR spectra are attributed to the typical skeletal stretching modes like C(sp<sup>2</sup>)-N and C(sp<sup>2</sup>)=N in the CN heterocycles, and the peak visible near 810 cm<sup>-1</sup> is identified as the bending vibration of s-triazine units. Note that, compared with both bulk g-C<sub>3</sub>N<sub>4</sub> and H-g-C<sub>3</sub>N<sub>4</sub>/C, the corresponding characteristic peaks on 3D g-C<sub>3</sub>N<sub>4</sub>/C-NS are much sharper and more intense, indicating more exposed surface functional groups are formed due to its graphene-like laminar structure and enlarged surface area. These exposed surface functional groups such as amino groups would be valuable for CO<sub>2</sub> molecule adsorption which may promote CO<sub>2</sub> photoreduction efficiency on the 3D g-C<sub>3</sub>N<sub>4</sub>/C-NS.

The chemical composition and chemical status of the constituent elements which are important in co-relating the catalytic activity of samples were studied by XPS. As shown in Fig. 4b, the full scan spectra of 3D g-C<sub>3</sub>N<sub>4</sub>/C-NS, H-g-C<sub>3</sub>N<sub>4</sub>/C and bulk g-C<sub>3</sub>N<sub>4</sub> reveal the existence of carbon (C 1s, 285 eV), nitrogen (N 1s, 400 eV) and oxygen (O 1s, 532 eV), agreeing well with the EDX data. The typical high resolution XPS spectra of C 1s, N 1s and O 1s in different samples are also given in Fig. 4c–e, respectively. In the case of bulk g-C<sub>3</sub>N<sub>4</sub> and H-g-C<sub>3</sub>N<sub>4</sub>/C, the C 1s XPS spectra have two main peaks at binding energies of 284.6 and 287.6 eV. The first peak at 284.6 eV is assigned to carbon impurities, and the second peak at 287.6 eV is ascribed to sp<sup>2</sup>-bonded carbon in N-containing aromatic rings (N–C=N) [47]. An additional small peak appeared at about 286.3 eV for H-g-C<sub>3</sub>N<sub>4</sub>/C should be attributed to C=N bonds which originates from the hybrid carbon [48]. Compared with H-g-C<sub>3</sub>N<sub>4</sub>/C sample, the C 1s XPS spectrum of 3D g-C<sub>3</sub>N<sub>4</sub>/C-NS exhibits two new peaks appearing at 285.4 and 288.7 eV, which represent the C combined with O in the form of C–O, C=O, and O–C=O groups according to the literature [49], indicating the existence of partial oxidation of C element in the 3D g-C<sub>3</sub>N<sub>4</sub>/C-NS. These

electron-withdrawing carbon-oxygen groups play a significant role in improving the separation efficiency of photogenerated electrons and holes during photocatalysis [50,51]. In Fig. 4d, the high resolution N 1s XPS spectra of both bulk g-C<sub>3</sub>N<sub>4</sub> and H-g-C<sub>3</sub>N<sub>4</sub>/C can be decomposed into four different Gaussian–Lorentzian peaks centered at 398.2, 398.9, 400.3 and 404.2 eV, which are respectively corresponded to sp<sup>2</sup> N bonded to C (C–N=C, pyridinic N), the tertiary N (N–C<sub>3</sub>, pyrrolic N), graphitic N & C–N–H, and terminal amino groups (–NH<sub>2</sub>). However, in case of 3D g-C<sub>3</sub>N<sub>4</sub>/C-NS, the peaks belonging to N 1s at 398.9 and 400.3 eV separately shift to higher binding energies of 399.6 and 400.8 eV, which indicates the presence of strong interaction between hybrid carbon and g-C<sub>3</sub>N<sub>4</sub> after carbothermal activation. The surface C/N ratio (atomic) for 3D g-C<sub>3</sub>N<sub>4</sub>/C-NS (1.07) is higher than H-g-C<sub>3</sub>N<sub>4</sub>/C (0.83), which is in accordance with the result of elemental analyzer (Table 1). The O 1s spectrum of bulk g-C<sub>3</sub>N<sub>4</sub> shown in Fig. 4e could be divided into two peaks at binding energies of 532.4 eV and 533.8 eV, which can be ascribed to C–OH groups and adsorbed O<sub>2</sub>, respectively. Different from the bulk g-C<sub>3</sub>N<sub>4</sub>, a new peak at about 531.3 eV appears in the O 1s spectrum of H-g-C<sub>3</sub>N<sub>4</sub>/C, which is regarded as the formation of N–C–O species [52]. Notably, the relative intensity of O 1s signal is significantly increased after carbothermal activation, indicating that more oxygen-containing functional groups not simply as adsorbed water are generated in 3D g-C<sub>3</sub>N<sub>4</sub>/C-NS.

### 3.2. CO<sub>2</sub> Photoreduction activity and mechanism study

The photocatalytic performance of as-prepared samples was evaluated by gas-phase CO<sub>2</sub> photoreduction experiments under simulated solar irradiation. Control experiments were conducted without photocatalyst or light irradiation, and no product was found, thus confirming that both photocatalyst and light irradiation are two essential conditions for the CO<sub>2</sub> photoreduction. Fig. 5 illustrates the evolution curves of two main products as functions of irradiation time over all samples, the yields of CO and CH<sub>4</sub> both increase with the prolonging of irradiation time, and the CO formation is more favorable than CH<sub>4</sub>

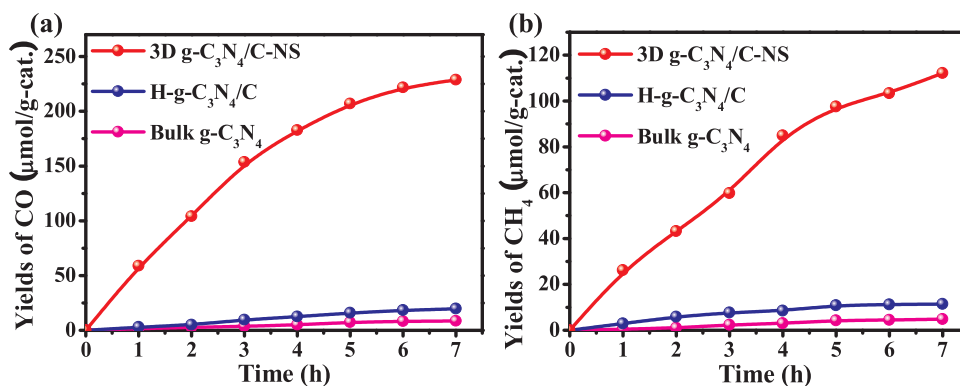


Fig. 5. Yields of CO (a) and CH<sub>4</sub> (b) as functions of irradiation time over the 3D g-C<sub>3</sub>N<sub>4</sub>/C-NS, H-g-C<sub>3</sub>N<sub>4</sub>/C and bulk g-C<sub>3</sub>N<sub>4</sub>.

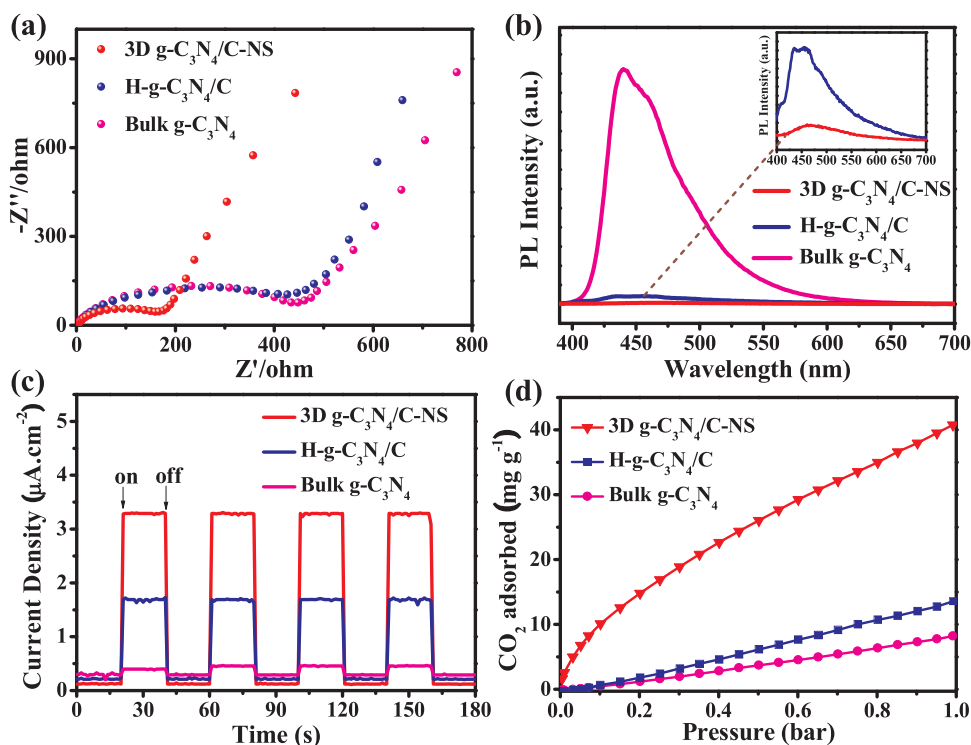


Fig. 6. (a) EIS profiles, (b) PL spectra, (c) photocurrent response and (d) CO<sub>2</sub> adsorption isotherms at 30 °C for the 3D g-C<sub>3</sub>N<sub>4</sub>/C-NS, H-g-C<sub>3</sub>N<sub>4</sub>/C and bulk g-C<sub>3</sub>N<sub>4</sub>.

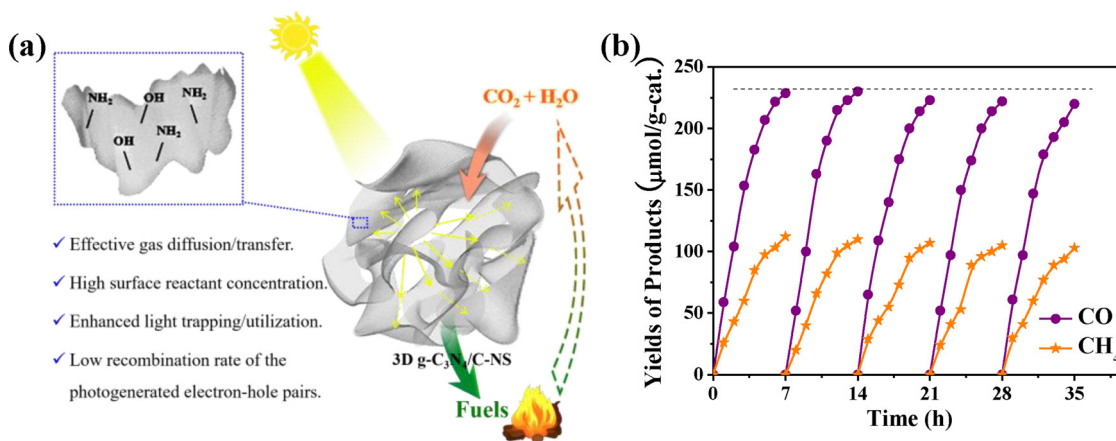


Fig. 7. (a) Depiction of the 3D g-C<sub>3</sub>N<sub>4</sub>/C-NS used in the photocatalytic reduction of CO<sub>2</sub> with H<sub>2</sub>O to produce value-added fuels, (b) Cyclic photocatalytic performance of 3D g-C<sub>3</sub>N<sub>4</sub>/C-NS under simulated solar irradiation.



formation on all samples. Similar to the result in our previous work, the H-g-C<sub>3</sub>N<sub>4</sub>/C exhibits a slight better photocatalytic activity (2 times) than the bulk g-C<sub>3</sub>N<sub>4</sub> because of the introduction of hybrid carbon. Interestingly, after carbothermal activation the 3D g-C<sub>3</sub>N<sub>4</sub>/C-NS exhibits a dramatically enhanced photocatalytic performance for CO<sub>2</sub> reduction with CO and CH<sub>4</sub> yield of 229 and 112 μmol g<sup>-1</sup>·cat., respectively, after 7 h of simulated solar irradiation, both values are about 12.5 times higher than the products over H-g-C<sub>3</sub>N<sub>4</sub>/C, respectively, which ascertains the importance of carbothermal activation for H-g-C<sub>3</sub>N<sub>4</sub>/C sample. Additionally, to determine whether other possible carbon sources in the 3D g-C<sub>3</sub>N<sub>4</sub>/C-NS will generate CO and CH<sub>4</sub> during the reaction, another control experiment by using Ar instead of CO<sub>2</sub> was made in the photocatalytic process according to the experimental condition. The result of gas chromatographic analysis demonstrates that no CO or CH<sub>4</sub> produces in the absence of CO<sub>2</sub> even after the irradiation time of 7 h, indicating that the carbon sources in CO and CH<sub>4</sub> are originated from the photoreduction of CO<sub>2</sub> on the 3D g-C<sub>3</sub>N<sub>4</sub>/C-NS. The products were also analyzed by gas chromatograph equipped with a thermal conductivity detector (TCD), where O<sub>2</sub> could be detected. Under simulated solar irradiation, the dominating reactions involved in the photocatalytic reduction of CO<sub>2</sub> with H<sub>2</sub>O to produce CO and CH<sub>4</sub> are summarized as follows [53,54]:



As shown from the Eqs. (1)–(4), the electrons (e<sup>-</sup>) and holes (h<sup>+</sup>) generated by the light irradiation are the key factors for this photocatalytic reaction. Electrons excited from the VB to the CB react with CO<sub>2</sub> molecules (which are adsorbed on the catalyst surface) to produce CO and CH<sub>4</sub>, while the holes remaining on the VB could oxidize H<sub>2</sub>O to form oxygen (O<sub>2</sub>). Photocatalytic reduction of CO<sub>2</sub> is a process of multi-electron steps, the formation of 1CO and 1CH<sub>4</sub> respectively require 2 and 8 electrons, and 4 holes are needed to generate 1O<sub>2</sub> molecule. Thus, not only CO and CH<sub>4</sub> are produced in the process of CO<sub>2</sub> photoreduction, but also O<sub>2</sub> is formed simultaneously. On the other hand, the concentration of gas reactants (especially CO<sub>2</sub>) on the photocatalyst surface is also an crucial factor to affect the efficiency of CO<sub>2</sub> photoreduction reaction (Eqs. (3,4)). Therefore, the excellent photocatalytic activity of the 3D g-C<sub>3</sub>N<sub>4</sub>/C-NS may attribute to its reduced recombination of photogenerated electron-hole pairs and enhanced CO<sub>2</sub> adsorption/activation on the surface of photocatalyst.

To provide sufficient evidences and examine the above assumed mechanism for the enhancement of CO<sub>2</sub> photocatalytic reduction performance, the effects of the 3D g-C<sub>3</sub>N<sub>4</sub>/C-NS structure on the kinetics of interfacial charge transfer were analyzed by Electrochemical impedance spectroscopy (EIS) measurement. The photoelectrode-to-electrolyte charge-transfer resistance (CTR), or equivalently, the efficiency in transport and separation of photogenerated electron-hole pairs, is represented by the semicircle diameter on the Nyquist plots at lower frequency [55,56]. As showed in Fig. 6a, the electrode arc-radius is much smaller for the 3D g-C<sub>3</sub>N<sub>4</sub>/C-NS compared with H-g-C<sub>3</sub>N<sub>4</sub>/C and bulk g-C<sub>3</sub>N<sub>4</sub>, indicating the decrease of CTR for 3D porous nanosheets composite, which will accelerate charge migration and separation so as to reduce energy-wasting recombination. As well as, a better separation rate of the produced electron/hole pairs activated by the photons was revealed by PL emission spectra. In general, a lower PL intensity indicates a weakened recombination rate of photogenerated charge carriers. As presented in Fig. 6b, upon the excitation at 330 nm, the main emission peak of bulk g-C<sub>3</sub>N<sub>4</sub> was observed at around 450 nm, which is in accordance with the band gap of g-C<sub>3</sub>N<sub>4</sub> (2.7 eV). Obviously, there is a significantly decrease in the PL intensity of both g-C<sub>3</sub>N<sub>4</sub>/C composites

compared to that of bulk g-C<sub>3</sub>N<sub>4</sub>, especially for the 3D g-C<sub>3</sub>N<sub>4</sub>/C-NS. The process can be assumed that the electrons are excited from the valence band to the conduction band and then transferred to hybrid carbon which serves as good conductor of electricity, preventing a direct recombination of electrons and holes. The further lower PL intensity of 3D g-C<sub>3</sub>N<sub>4</sub>/C-NS compared with H-g-C<sub>3</sub>N<sub>4</sub>/C can be ascribed to the decrease in the thickness of nanosheets associated with the quantum confinement effect with conduction and valence bands shifting in opposite directions [38]. The higher charge transfer efficiency and more efficient separation of photogenerated electron-hole pairs for the 3D g-C<sub>3</sub>N<sub>4</sub>/C-NS were also confirmed by its photocurrent response shown in Fig. 6c. The photocurrent density of 3D g-C<sub>3</sub>N<sub>4</sub>/C-NS is about 3.3 μA cm<sup>-2</sup>, which is much larger than that of H-g-C<sub>3</sub>N<sub>4</sub>/C (1.6 μA cm<sup>-2</sup>) and bulk g-C<sub>3</sub>N<sub>4</sub> (0.4 μA cm<sup>-2</sup>). These data adequately prove that such 3D porous nanosheets with improved textural properties can promote the photo-generated charge mobility efficiently and react with the target immediately, thus leading to the enhancement of photocatalytic performance. In addition, CO<sub>2</sub> adsorption ability on the surface of above mentioned samples was evaluated through equilibrium CO<sub>2</sub> adsorption isotherm at 30 °C. As demonstrated in Fig. 6d, the 3D g-C<sub>3</sub>N<sub>4</sub>/C-NS presents a higher CO<sub>2</sub> adsorption capacity (40.8 mg g<sup>-1</sup>) than that of H-g-C<sub>3</sub>N<sub>4</sub>/C (13.6 mg g<sup>-1</sup>) and bulk g-C<sub>3</sub>N<sub>4</sub> (8.3 mg g<sup>-1</sup>) at 1.0 bar. The enhanced CO<sub>2</sub> adsorption ability for the 3D g-C<sub>3</sub>N<sub>4</sub>/C-NS should be attributed to its more exposed surface functional groups because of the enlarged surface area, as confirmed by the FTIR result.

As a result of various experiments, we consider that the excellent photocatalytic performance of the 3D g-C<sub>3</sub>N<sub>4</sub>/C-NS mainly benefits from their favorable properties induced by its unique structures. Firstly, 3D porous architecture with hierarchical mesostructure promotes the effective transportation of gas reactants to photoactive sites and accelerates the diffusion of the products. Meanwhile, the formed plentiful surface functional groups like amino groups on the 3D g-C<sub>3</sub>N<sub>4</sub>/C-NS due to its graphene-like laminar structure and enlarged surface area would be favorable to CO<sub>2</sub> molecule adsorption and provide a high reactant concentration on the surface of photocatalyst. Secondly, graphene-like nanosheets with 3D interconnecting structure can serve as efficient light management to increase the light harvesting inside active sites of photocatalyst. On the other hand, multiple light scattering among transparent ultrathin graphene-like nanosheets will further increase the utilization rate of the trapped light during photocatalytic process (Fig. 7a). More importantly, the photo-induced electrons in the g-C<sub>3</sub>N<sub>4</sub> can effectively drift to the hybrid carbon under their inner electric field because of the quantum confinement effect of graphene-like nanosheets. This is helpful for the reduction of electron-hole pair recombination and prolongs the lifetime of photoexcited charge carriers. Finally, XPS analysis confirms that the existence of partial electron-withdrawing carbon-oxygen groups (such as C–O, C=O, and O–C=O groups) on the surface of 3D g-C<sub>3</sub>N<sub>4</sub>/C-NS after carbothermal activation will lead to an easier electron flow on the external surface of photocatalyst and thus can greatly suppress the recombination of the photogenerated electron-hole pairs. All above extraordinary characteristics together contribute to the significant improvement in photocatalytic performance of 3D porous g-C<sub>3</sub>N<sub>4</sub>/C nanosheets composite catalyst.

The stability of a photocatalyst is also very important with respect to its practical application. Herein, the CO<sub>2</sub> photoreduction reaction over 3D g-C<sub>3</sub>N<sub>4</sub>/C-NS was repeated up to five times under the same experimental conditions, where the illumination time was set to 7 h for every cycle. As can be seen from Fig. 7b, no apparent deactivation was observed even if after five consecutive runs (the CO<sub>2</sub> photoreduction efficiency declined by only about 3%), indicating that the obtained 3D g-C<sub>3</sub>N<sub>4</sub>/C-NS possesses excellent stability during the gas-phase CO<sub>2</sub> photocatalytic reaction.

## 4. Conclusion

In summary, we have synthesized 3D porous g-C<sub>3</sub>N<sub>4</sub>/C nanosheets composite for the first time through a simple pyrolysis and subsequent carbothermal activation method using a mixture of melamine and natural soybean oil as precursor. The key feature of this 3D porous architecture is that the formed ultrathin graphene-like g-C<sub>3</sub>N<sub>4</sub>/C nanosheets have crumpled morphology and hierarchical mesostructure, leading to a high surface area and large pore volume. Photocatalytic measurements reveal that the obtained 3D porous g-C<sub>3</sub>N<sub>4</sub>/C nanosheets composite exhibits an exceptionally higher activity than bulk g-C<sub>3</sub>N<sub>4</sub> in the photocatalytic reduction of CO<sub>2</sub> with H<sub>2</sub>O vapor. The further analysis suggests that the remarkably increased photocatalytic performance is mainly attributed to its improved textural properties, enhanced light trapping/utilization, high-efficient CO<sub>2</sub> adsorption ability and low recombination of the photogenerated electron-hole pairs. This study not only presents a possibility of using 3D porous g-C<sub>3</sub>N<sub>4</sub>/C nanosheets as efficient photocatalyst for conversion of CO<sub>2</sub>, but also provides an optional effective method to synthesize other 3D porous carbon composites for energy and environmental applications.

## Acknowledgements

This work was carried out with financial supports from National Natural Science Foundation of China (Grant No. 21103024 and No. 61171008), Yancheng Huanbo Energy Technonogy Limited Company, Longyuan Youth Innovative Talents Program, and Technology Development Project of Jiaying University.

## Appendix A. Supplementary data

Supplementary material related to this article can be found, in the online version, at doi:<https://doi.org/10.1016/j.apcatb.2018.08.018>.

## References

- [1] T. Inoue, A. Fujishima, S. Konishi, K. Honda, *Nature* 277 (1979) 637–638.
- [2] R. Silva, D. Voiry, M. Chhowalla, T. Asefa, *J. Am. Chem. Soc.* 135 (2013) 7823–7826.
- [3] M.J. Ju, J.C. Kim, H.-J. Choi, I.T. Choi, S.G. Kim, K. Lim, J. Ko, J.-J. Lee, I.-Y. Jeon, J.-B. Baek, *ACS Nano* 7 (2013) 5243–5250.
- [4] W. Peng, S. Liu, H. Sun, Y. Yao, L. Zhi, S. Wang, *J. Mater. Chem. A Mater. Energy Sustain.* 1 (2013) 5854–5859.
- [5] H. Sun, S. Liu, G. Zhou, H.M. Ang, M.O. Tadé, S. Wang, *ACS Appl. Mater. Inter.* 4 (2012) 5466–5471.
- [6] H. Sun, Y. Wang, S. Liu, L. Ge, L. Wang, Z. Zhu, S. Wang, *Chem. Commun. (Camb.)* 49 (2013) 9914–9916.
- [7] G. Liu, P. Niu, C. Sun, S.C. Smith, Z. Chen, G.Q. Lu, H.-M. Cheng, *J. Am. Chem. Soc.* 132 (2010) 11642–11648.
- [8] M. Shalom, S. Inal, C. Fettekenhauer, D. Neher, M. Antonietti, *J. Am. Chem. Soc.* 135 (2013) 7118–7121.
- [9] K. Maeda, K. Sekizawa, O. Ishitani, *Chem. Commun. (Camb.)* 49 (2013) 10127–10129.
- [10] J. Lin, Z. Pan, X. Wang, *ACS Sustain. Chem. Eng.* 2 (2013) 353–358.
- [11] A. Kudo, Y. Miseki, *Chem. Soc. Rev.* 38 (2009) 253–278.
- [12] J. Hong, W. Zhang, Y. Wang, T. Zhou, R. Xu, *ChemCatChem* 6 (2014) 2315–2321.
- [13] X. Wang, K. Maeda, A. Thomas, K. Takanabe, G. Xin, J.M. Carlsson, K. Domen, M. Antonietti, *Nat. Mater.* 8 (2009) 76–80.
- [14] B. Chai, T. Peng, J. Mao, K. Li, L. Zan, *Phys. Chem. Chem. Phys.* 14 (2012) 16745–16752.
- [15] J. Liu, Y. Zhang, L. Lu, G. Wu, W. Chen, *Chem. Commun. (Camb.)* 48 (2012) 8826–8828.
- [16] Y. Zhang, J. Liu, G. Wu, W. Chen, *Nanoscale* 4 (2012) 5300–5303.
- [17] J. Hong, X. Xia, Y. Wang, R. Xu, *J. Mater. Chem.* 22 (2012) 15006–15012.
- [18] S. Yan, Z. Li, Z. Zou, *Langmuir* 26 (2010) 3894–3901.
- [19] S. Yan, Z. Li, Z. Zou, *Langmuir* 25 (2009) 10397–10401.
- [20] Y. Wang, Z. Wang, S. Muhammad, J. He, *CrystEngComm* 14 (2012) 5065–5070.
- [21] G. Zhang, J. Zhang, M. Zhang, X. Wang, *J. Mater. Chem.* 22 (2012) 8083–8091.
- [22] J. Zhang, M. Zhang, R.Q. Sun, X. Wang, *Angew. Chem.* 124 (2012) 10292–10296.
- [23] J. Tian, R. Ning, Q. Liu, A.M. Asiri, A.O. Al-Youbi, X. Sun, *ACS Appl. Mater. Inter.* 6 (2014) 1011–1017.
- [24] Y. Jiao, Y. Zheng, M. Jaroniec, S.Z. Qiao, *J. Am. Chem. Soc.* 136 (2014) 4394–4403.
- [25] E. Kroke, M. Schwarz, E. Horath-Bordon, P. Kroll, B. Noll, A.D. Norman, *New J. Chem.* 26 (2002) 508–512.
- [26] H. Zhao, H. Yu, X. Quan, S. Chen, Y. Zhang, H. Zhao, H. Wang, *Appl. Catal. B: Environ.* 152 (2014) 46–50.
- [27] A.K. Geim, K.S. Novoselov, *Nat. Mater.* 6 (2007) 183–191.
- [28] X. Zhang, X. Xie, H. Wang, J. Zhang, B. Pan, Y. Xie, *J. Am. Chem. Soc.* 135 (2012) 18–21.
- [29] P. Niu, L. Zhang, G. Liu, H.M. Cheng, *Adv. Funct. Mater.* 22 (2012) 4763–4770.
- [30] N. Cheng, J. Tian, Q. Liu, C. Ge, A.H. Qusti, A.M. Asiri, A.O. Al-Youbi, X. Sun, *ACS Appl. Mater. Inter.* 5 (2013) 6815–6819.
- [31] W.-J. Ong, M.M. Gui, S.-P. Chai, A.R. Mohamed, *RSC Adv.* 3 (2013) 4505–4509.
- [32] X. Bai, L. Wang, Y. Wang, W. Yao, Y. Zhu, *Appl. Catal. B: Environ.* 152 (2014) 262–270.
- [33] W.-J. Ong, L.-L. Tan, S.-P. Chai, S.-T. Yong, A.R. Mohamed, *Nano Res.* 7 (2014) 1528–1547.
- [34] S.M. Lyth, Y. Nabae, S. Moriya, S. Kuroki, M.-A. Kakimoto, J.-I. Ozaki, S. Miyata, *J. Phys. Chem. C* 113 (2009) 20148–20151.
- [35] S. Lyth, Y. Nabae, N. Islam, S. Kuroki, M. Kakimoto, S. Miyata, *J. Electrochem. Soc.* 158 (2011) 194–201.
- [36] J. Liu, Y. Liu, N. Liu, Y. Han, X. Zhang, H. Huang, Y. Lifshitz, S.-T. Lee, J. Zhong, Z. Kang, *Science* 347 (2015) 970–974.
- [37] Y. Wang, X. Bai, H. Qin, F. Wang, Y. Li, X. Li, S. Kang, Y. Zuo, L. Cui, *ACS Appl. Mater. Inter.* 8 (2016) 17212–17219.
- [38] J. Xu, L. Zhang, R. Shi, Y. Zhu, *J. Mater. Chem. A* 1 (2013) 14766–14772.
- [39] S. Yang, Y. Gong, J. Zhang, L. Zhan, L. Ma, Z. Fang, R. Vajtai, X. Wang, P.M. Ajayan, *Adv. Mater.* 25 (2013) 2452–2456.
- [40] G. Liao, S. Chen, X. Quan, H. Yu, H. Zhao, *J. Mater. Chem.* 22 (2012) 2721–2726.
- [41] M. Groenewolt, M. Antonietti, *Adv. Mater.* 17 (2005) 1789–1792.
- [42] Z. Huang, F. Li, B. Chen, G. Yuan, *RSC Adv.* 5 (2015) 14027–14033.
- [43] S. Fang, Y. Xia, K. Lv, Q. Li, J. Sun, M. Li, *Appl. Catal. B: Environ.* 185 (2016) 225–232.
- [44] Q. Liang, Z. Li, X. Yu, Z.-H. Huang, F. Kang, Q.-H. Yang, *Adv. Mater.* 27 (2015) 4634–4639.
- [45] X. Men, H. Chen, K. Chang, X. Fang, C. Wu, W. Qin, S. Yin, *Appl. Catal. B: Environ.* 187 (2016) 367–374.
- [46] X. Hu, W. Xu, L. Zhou, Y. Tan, Y. Wang, S. Zhu, J. Zhu, *Adv. Mater.* 29 (2017) 1604031.
- [47] L. Wang, J. Ding, Y. Chai, Q. Liu, J. Ren, X. Liu, W.-L. Dai, *Dalton Trans.* 44 (2015) 11223–11234.
- [48] W.J. Ong, L.L. Tan, S.P. Chai, S.T. Yong, *Chem. Commun. (Camb.)* 51 (2015) 858–861.
- [49] Y. Hou, Z. Wen, S. Cui, X. Guo, J. Chen, *Adv. Mater.* 25 (2013) 6291–6297.
- [50] H. Xu, J. Yan, X. She, L. Xu, J. Xia, Y. Xu, Y. Song, L. Huang, H. Li, *Nanoscale* 6 (2014) 1406–1415.
- [51] H.-J. Li, B.-W. Sun, L. Sui, D.-J. Qian, M. Chen, *Phys. Chem. Chem. Phys.* 17 (2015) 3309–3315.
- [52] J. Li, B. Shen, Z. Hong, B. Lin, B. Gao, Y. Chen, *Chem. Commun.* 48 (2012) 12017–12019.
- [53] O.K. Varghese, M. Paulose, T.J. LaTempa, C.A. Grimes, *Nano Lett.* 9 (2009) 731–737.
- [54] T. Wang, X. Meng, G. Liu, K. Chang, P. Li, Q. Kang, L. Liu, M. Li, S. Ouyang, J. Ye, J. Mater. Chem. A 3 (2015) 9491–9501.
- [55] Y. Hou, F. Zuo, A. Dagg, P. Feng, *Angew. Chem. Int. Edit.* 52 (2013) 1248–1252.
- [56] S. Yu, L. Yang, Y. Tian, P. Yang, F. Jiang, S. Hu, X. Wei, J. Zhong, *J. Mater. Chem. A* 1 (2013) 12750–12758.